


Cite this: *RSC Adv.*, 2022, 12, 16419

Impact of atomic layer deposited TiO₂ on the photocatalytic efficiency of TiO₂/w-VA-CNT nanocomposite materials†

Inês E. Oliveira,^{ID a,c,d} Ricardo M. Silva,^{ID a} Joana Rodrigues,^{ID b} Maria R. Correia,^{ID b} Teresa Monteiro,^{ID b} Joaquim L. Faria,^{ID c,d} Rui F. Silva^{ID a} and Cláudia G. Silva^{ID *c,d}

Titanium oxide (TiO₂) has been widely investigated as a photocatalytic material, and the fact that its performance depends on its crystalline structure motivates further research on the relationship between preparation methods and material properties. In this work, TiO₂ thin films were grown on non-functionalized wave-like patterned vertically aligned carbon nanotubes (w-VA-CNTs) via the atomic layer deposition (ALD) technique. Grazing incidence X-ray diffraction (GIXRD) analysis revealed that the structure of the TiO₂/VA-CNT nanocomposites varied from amorphous to a crystalline phase with increasing deposition temperature, suggesting a "critical deposition temperature" for the anatase crystalline phase formation. On the other hand, scanning transmission electron microscopy (STEM) studies revealed that the non-functionalized carbon nanotubes were conformally and homogeneously coated with TiO₂, forming a nanocomposite while preserving the morphology of the nanotubes. X-ray photoelectron spectroscopy (XPS) provided information about the surface chemistry and stoichiometry of TiO₂. The photodegradation experiments under ultraviolet (UV) light on a model pollutant (Rhodamine B, RhB) revealed that the nanocomposite comprised of anatase crystalline TiO₂ grown at 200 °C (11.2 nm thickness) presented the highest degradation efficiency viz 55% with an illumination time of 240 min. Furthermore, its recyclability was also demonstrated for multiple cycles, showing good recovery and potential for practical applications.

Received 28th December 2021

Accepted 23rd May 2022

DOI: 10.1039/d1ra09410f

rsc.li/rsc-advances

Introduction

Atomic layer deposition (ALD) has been recognized as an effective synthesis method for designing catalytic materials with a tailored activity, selectivity and stability.¹ ALD provides a tool for conformal coating on high aspect-ratio nanostructures with excellent uniformity. It has become the method of choice for both template-directed nanofabrication and engineering of surface properties. As a matter of fact, there is a need for nanomaterials for environmental catalysis to efficiently treat wastewaters using photocatalytic processes powered *via*

sunlight and operating at room temperature (RT). Metal oxides are among the most used nanomaterials in photocatalytic reactions.²

Titanium dioxide (TiO₂) is one of the metal oxides that stands out as photocatalyst material mainly due to its high oxidizing power, inducing the generation of reactive oxygen species, low relative cost, photostability, non-toxicity and insolubility under most conditions. These characteristics make TiO₂ a very attractive material for environmental applications, especially in solar-driven degradation of organic pollutants in wastewater treatment.^{3,4} In general, the properties of TiO₂ are strongly dependent on the dimensionality and morphology, as well as on its amorphous/crystalline structure; it is, therefore, imperative to consider this feature prior to the application. This motivated the development of a great variety of synthetic routes for the fabrication of TiO₂ with well-defined morphologies at the micro and nanoscale, ranging from wet chemical to vapor phase methods.^{2,5,6}

The ALD technique stands out here by providing the controlled deposition of TiO₂ on materials with a large surface-to-volume ratio, where the deposited ultra-thin films are highly conformal and continuous to the underneath substrate, a consequence of its self-limiting nature.⁷ Hence, nanostructured TiO₂ combined with the tremendous specific

^aCICECO – Aveiro Institute of Materials, Department of Materials and Ceramic Engineering, University of Aveiro, 3810-193 Aveiro, Portugal

^bi3N, Department of Physics, University of Aveiro, 3810-193 Aveiro, Portugal

^cLaboratory of Separation and Reaction Engineering – Laboratory of Catalysis and Materials (LSRE-LCM), Faculty of Engineering, University of Porto, Rua Dr Roberto Frias s/n, 4200-465 Porto, Portugal. E-mail: cgsilva@fe.up.pt

^dALiCE – Associate Laboratory in Chemical Engineering, Faculty of Engineering, University of Porto, Rua Dr Roberto Frias, 4200-465 Porto, Portugal

† Electronic supplementary information (ESI) available: Experimental apparatus, additional TEM and SEM images, EDS mapping, GIXRD, regarding the deposition temperature variation, the XPS survey spectra of the coated and uncoated w-VA-CNTs and complementary photocatalytic studies. See <https://doi.org/10.1039/d1ra09410f>



surface achieved in vertically aligned carbon nanotubes (VA-CNTs) arrays seems to be a suitable solution to promote the enhancement in the photocatalytic activity of TiO_2 , resulting from the combination of both materials' physico-chemical properties.⁴ In contrast to ALD, the solution-based deposition techniques can cause the collapsing of the VA-CNTs arrays when the solution is removed, losing the potential benefits of the vertical alignment. Nevertheless, these techniques have been widely explored in preparing composites comprised of TiO_2 and commercial CNTs.^{5,8–11} However, the photocatalytic activity of TiO_2 can be affected by some physicochemical parameters, such as phase composition, film thickness, surface topography, chemical composition and presence of defects in the crystal lattice.¹² In addition to the amorphous phase, the polymorphs of the crystalline TiO_2 phase are anatase, rutile and brookite, which may exhibit different photocatalytic performances. Typically, the anatase TiO_2 phase exhibits the highest photocatalytic activity in photo-oxidation reactions, as is the case of photocatalytic degradation of organic pollutants.¹²

In the present work, an ALD process based on titanium tetraisopropoxide (TTIP) and water (H_2O) as reactive precursors is proposed for the TiO_2 synthesis on VA-CNTs, where *ex situ* oxidative treatments (*i.e.*, functionalization) of the CNTs are avoided. A homogeneous and conformal TiO_2 photocatalytic thin-film material is obtained either amorphous or crystalline.

In fact, TiO_2 ALD using TTIP as Ti source and H_2O was first reported by Ritala *et al.*¹³ Since then, TTIP has been explored as a good alternative to tetrachloride (TiCl_4), one of the most commonly used Ti precursors. However, the production of corrosive by-products is considered a drawback. In addition, the synthesis of TiO_2 crystalline structures based on TTIP and H_2O can be obtained at moderate deposition temperatures (*e.g.*, 250 °C), making it worth use.^{13–15} It is important to emphasize that insufficient covering of the nanotubes' surface is not unusual due to their chemically inert nature.

For this reason, it is usually necessary to introduce defects or new functional groups on their surface, employing oxidative pre-treatments and, therefore, facilitating the nucleation of the second material, for instance, metal oxides.^{16–19} Guerra-Núñez *et al.*⁷ used non-functionalized vertically aligned multiwall carbon nanotubes (VA-MWCNTs) to study the nucleation and growth of TiO_2 ALD thin films using TTIP and H_2O at 60, 120 and 220 °C, concluding that the TiO_2 film completely covered the surface of the CNTs with amorphous and crystalline phases. Nevertheless, such interesting work did not present any practical application of the obtained nanostructures.

Herein, the aim was to evaluate the photocatalytic performance for TiO_2 ALD on two types of VA-CNTs arrays: wave-like patterned (w-VA-CNTs) and planar (VA-CNTs), TiO_2 /w-VA-CNTs and TiO_2 /VA-CNTs nanocomposites, respectively. Apart from the CNT vertical alignment, the obtained spontaneous wave-like patterning VA-CNTs provide a surface waviness feature that could also be promising for enhancing photocatalytic activity. Moreover, the effect of TiO_2 loading (*i.e.*, ALD number of cycles) onto the surface of the nanotubes was investigated, as well as the deposition temperature towards the optimal photocatalytic

performance, which the TiO_2 thickness and crystalline structure can define. Finally, the prepared nanocomposites have been extensively characterized and tested as potential catalysts for photo-assisted water decontamination, using rhodamine B (RhB) as a model pollutant, validating their application in the photocatalysis research field. Fig. 1 illustrates a schematic of the photocatalytic nanocomposite materials presented in this article.

Experimental

TiO_2 atomic layer deposition

Single side polished Si wafer substrates from Siegert Wafer (Si (100)-orientation; for X-ray reflectometry (XRR) measurements), and Siltronix (Si/ SiO_2 300 nm; for VA-CNTs growth process and photocatalytic studies) were cut into 2 cm × 2 cm and 1 cm × 1 cm samples, which were used as a reference in the TiO_2 ALD process. Prior to the ALD process, both types of Si wafers were cleaned with a fresh 'piranha' solution (1 : 3 H_2O_2 / H_2SO_4 mixture) for 30 minutes, rinsed with distilled water, and dried with compressed air.

TiO_2 thin films were directly deposited onto Si substrates, VA-CNTs and w-VA-CNTs *via* conventional thermal ALD. The film thickness was measured from the Si substrate coated simultaneously with the VA-CNTs arrays. These two types of CNTs arrays were grown by thermal chemical vapor deposition (TCVD) on Si/ SiO_2 substrates, for a period of 15 min, at 700 and 650 °C, respectively. From the experimental point of view, the wave-like pattern was obtained by modulating the TCVD growing temperature, from a gas mixture of C_2H_2 (10 sccm)/ H_2 (400 sccm)/Ar (100 sccm) using Ni as a catalyst. Ni catalyst thin film of 12 nm thickness was sputter deposited (DC, sputtering gas: Ar) onto Si/ SiO_2 substrates, as reported elsewhere.²⁰ The nanotube arrays present an average height of $2.2 \pm 0.1 \mu\text{m}$ for VA-CNTs and $2.3 \pm 0.1 \mu\text{m}$ for w-VA-CNTs.

The TiO_2 ALD process was carried out in a tubular home-made ALD reactor. TiO_2 thin films were deposited onto VA-CNTs and w-VA-CNTs arrays at different temperatures, ranging from 150 to 300 °C. The depositions were carried out at 100, 150, 200, 250 and 300 °C for up to 200 cycles. Titanium(IV) tetraisopropoxide (TTIP, STREM Chemicals, 98% purity, used as received) and deionized water (H_2O , Milli-Q) were used as metal and oxygen precursors, respectively. The precursors were

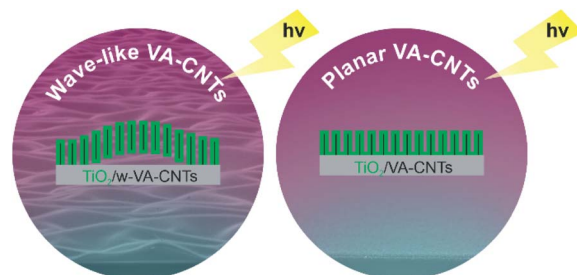


Fig. 1 Schematic representation of the photocatalytic TiO_2 /w-VA-CNTs and TiO_2 /VA-CNTs nanocomposites produced in this work.



introduced into the reaction chamber with pneumatic valves from their reservoirs, where the TTIP reservoir was heated to 80 °C, and the H₂O reservoir was kept at RT. TTIP was held at 80 °C to provide sufficient Ti precursor vapours in the reactor chamber. Additionally, all the delivery tubing lines were heated at 100 °C to avoid precursor condensation throughout the deposition process. Pure argon (Ar) served both as the carrier and purging gas, and a total flow rate of 50 sccm was used, leading to an operating pressure of 0.24 kPa during the precursor pulse timing. In practice, each ALD cycle involves at least four separate steps: (i) exposure to the metal precursor; (ii) purge of the excess precursor; (iii) exposure to the deionized water (*i.e.*, exposure to an oxidizer to form an oxide); and (iv) purge of the water prior to metal precursor exposure. In a typical ALD run, each cycle consisted of 0.5 s TTIP pulse, 20 s of residence time, 10 s Ar purging, 2 s H₂O pulse, 15 s of residence time, 10 s Ar purging. These experimental parameters were selected according to a preliminary set of depositions and literature review.^{13,15} Several samples of TiO₂/VA-CNTs nanocomposites with different TiO₂ thicknesses were prepared by varying the number of ALD cycles (50, 100, 200 and 400). Fig. S1 (ESI[†]) shows a schematic illustration of the TiO₂ depositions on VA-CNTs with different morphologies, and Fig. S2[†] shows macrographs of the physical appearance of the VA-CNTs after TiO₂ ALD.

Materials characterization

The crystallinity of TiO₂ thin films deposited at different temperatures on VA-CNTs arrays was investigated by grazing incidence X-ray diffraction (GIXRD) using the Cu K α radiation (λ = 1.54060 Å) and a step size of 0.02° with an incident angle of 1.5°. The phase analysis of the prepared samples was carried out using a PANalytical X'Pert Pro system. Based on the Debye–Scherrer equation, the mean crystallite size was determined from the full width at half maximum (FWHM) of the most intense diffraction maxima.²¹ The thickness of TiO₂ films deposited on the Si wafer substrates was measured by XRR using a PANalytical diffractometer. This diffractometer was equipped with a Cu K α source powered at 45 kV/40 mA. The surface topography of the TiO₂ films deposited on the Si/SiO₂ wafer substrates was imaged by atomic force microscopy (AFM) using a Ntegra Prima set-up (NT-MDT) in tapping mode under ambient conditions. A silicon cantilever (Nanosensor PPP-NCHR) with a spring constant of $k \approx 42$ N m⁻¹ and tip radius < 10 nm was used. Surface roughness was determined as root-mean-square value (R_q).

Wettability measurements were performed with the aid of a commercial contact angle system (Dataphysics OCA) using deionized water (H₂O, Milli-Q, drop volume 3 μ L) to evaluate the contact angle at room temperature.

Structural and morphological properties of TiO₂/VA-CNTs nanocomposites were characterized by scanning electron microscopy (SEM) (Hitachi SU70), operated at 15 kV and equipped with energy-dispersive X-ray spectroscopy (EDS). SEM images were obtained in the secondary-electron image mode at an accelerating voltage of 15 kV.

Further morphological details of the coated carbon nanotubes were investigated by scanning transmission electron microscopy (STEM, Hitachi HD2700), operated at 200 kV and equipped with EDS (Bruker) for elemental analysis. The samples for STEM studies were prepared by carefully contacting a holey carbon grid throughout the nanocomposite samples. The growth rate (*i.e.*, growth per cycle (GPC)) was obtained from the film thickness of the TiO₂ on the surface of the nanotubes divided by the number of ALD cycles. The TiO₂ film thickness estimation was determined from the scanning transmission electron microscopy (TE-STEM mode) images by directly measuring the TiO₂ film on the surface of the nanotubes.

RT μ -Raman spectroscopy was carried out to assess the degree of crystallinity of the as-grown carbon nanotubes and TiO₂. The Raman measurements were conducted on a Horiba Jobin Yvon HR800 spectrometer under a 532 nm laser line (Ventus-LP-50085, Material Laser Quantum), focusing with an objective of $\times 50$ magnification, and using an ND 0.6 neutral density filter to avoid photo-induced phase conversion during the measurements.

The steady-state photoluminescence (PL) and PL excitation (PLE) measurements were carried out at RT using a Fluorolog-3 Horiba Scientific set-up with a double additive grating Gemini 180 monochromator (1200 grooves mm⁻¹ and 2×180 mm) in the excitation and a triple grating iHR550 spectrometer in the emission (1200 grooves mm⁻¹ and 550 mm), using a 450 W Xe lamp as the excitation source. Photon energy above or nearly equal to the bandgap of the TiO₂ anatase phase (~ 3.2 eV at RT, indirect bandgap²²) was employed for the excitation. Since the PL signal was seen to be relatively low, both excitation and detection slits were kept at 7 nm (nearly the maximum allowed by the equipment). The PLE spectra were acquired by fixing the detector on the maximum of the observed optical centre(s).

The absorbance and diffuse reflectance properties of the TiO₂ deposited on the w-VA-CNTs nanocomposites were determined by UltraViolet-Visible spectrophotometry (UV-Vis) (Shimadzu LISR-3100 UV-Vis-NIR) in the range of 200–600 nm. A BaSO₄ flat disk was used as a reference.

To determine the exact chemical composition of the TiO₂ thin films deposited over the carbon nanotubes, X-ray photoelectron spectroscopy (XPS) measurements were performed in an ultrahigh-vacuum system with a 2×10^{-10} mbar base pressure. The system is fitted with a hemispherical electron energy analyser (SPECS Phoibos 150), a delay-line detector and a monochromatic AlK α (1486.74 eV) X-ray source. High-resolution spectra were recorded at normal emission take-off angle and with a pass-energy of 20 eV, affording a 0.5 eV overall instrumental peak broadening. XPS spectra were deconvoluted using XPSPeak4.1 software using Gaussian–Lorentzian (G–L) fitting functions after Shirley-type background subtraction. The binding energy of each element was calibrated using the C 1s peak (284.6 eV).

Photocatalytic experiments

All the nanocomposites were tested towards the photocatalytic degradation of RhB, to study the influence of the VA-CNTs

surface waviness feature and TiO₂ crystallinity on the photocatalytic activity of the nanocomposite materials. The experiments were carried out in a cylindrical glass reactor filled with 20 mL of a 5 mg L⁻¹ RhB aqueous solution with a pH value of 5.3. The solution was continuously purged with an airflow. A 10 W UV-LED emitting at 365 nm was used as the excitation source. The nanocomposite samples with a geometrical area of 1 cm × 1 cm were kept apart from the excitation source by 1 cm, as schematically illustrated in Fig. S3.† The temperature and pH of the solution were measured before and after each photocatalytic reaction. Initial values are room temperature (24 °C) and pH value 5.3. After 240 min of irradiation time, the temperature of the solution was changed to 30 °C and the pH to 5.7. In order to achieve the adsorption–desorption equilibrium, the solution was continuously stirred, in the dark, for 30 min. Then, the solution was irradiated for 240 minutes. Throughout the reaction and at certain times, solution samples were collected to assess the concentration variation of RhB dye by UV-Vis absorption spectroscopy measurements. RhB is a fluorescent dye belonging to the group of xanthene dyes, presenting an absorption maximum of around 555 nm associated with the RhB $\pi \rightarrow \pi^*$ transitions.²³ The degradation of RhB was assessed in terms of C/C_0 evolution, where C_0 is the initial RhB concentration of the solution before turning on the excitation light and C is the concentration of RhB in the solution at a certain illumination time. Assuming pseudo-first-order kinetics, $\ln(C_0/C)$ was plotted vs. time (min), and the linear regression slope represents the kinetic constant. The recyclability of the nanocomposite was evaluated, by repeating the photo-degradation tests four times, with a fresh dye solution. In detail, at the end of each degradation cycle, the nanocomposite sample was immersed in deionized water for a few minutes and then dried in a furnace at 60 °C overnight. The nanocomposite sample was again characterized by GIXRD, SEM with the corresponding EDS elemental mapping, and Raman spectroscopy after the photocatalytic tests to verify the mechanical, chemical and photostability of the material.

Results and discussion

TiO₂ deposition over carbon nanotubes by ALD

The as-prepared non-functionalized w-VA-CNTs arrays were coated with 200 TiO₂ ALD cycles at 100, 150, 200, 250 and 300 °C. The primary purpose of this series of nanocomposites was to investigate the impact of various deposition temperatures of TiO₂ films on surface morphology and phase composition and their subsequent influence on the photodegradation of the RhB organic dye.

Amorphous-to-crystalline phase transition of TiO₂ thin films happens in a range of deposition temperatures depending on the preparation methods since TiO₂ thin films mainly exhibit amorphous, anatase or rutile structures. For instance, Huang *et al.* reported the decoration of acid-treated CNTs (*i.e.*, functionalized CNTs) with anatase TiO₂ ALD nanoparticles from the reaction of TiCl₄ with H₂O. The authors claimed that these TiO₂ nanoparticles with the anatase phase could be directly formed on CNTs by ALD at 300 °C.²⁴

The high- and low-magnified SEM images (Fig. 2a and b) show the surface morphology and vertical alignment of the w-VA-CNTs nanocomposites after 200 ALD cycles. From the representative SE-STEM and ZC-TEM mode images (Fig. 2c–f), it can be observed that the nanotubes are coated with a uniform and homogeneous layer of TiO₂ (see also Fig. S4†). There are no significant differences between the morphology of the outer surface of the two carbon nanotubes (Fig. 2e and f), with the presence of TiO₂ corresponding to the brighter contrast along the nanotubes. The observed bright contrast regions arise from the heavier (Z-contrast) Ti atoms in TiO₂, proving that the nanotube is coated with a material of larger electronic density. The assignment is consistent with the chemical analysis by EDS elemental mapping (Fig. S4†). The STEM observations suggest the successful coating of the non-functionalized w-VA-CNTs by the ALD process while their original shape is preserved. This finding is also supported by the EDS elemental mapping investigation (Fig. S5 and Table S1†) of the nanocomposites, revealing that the TiO₂ was homogeneously distributed over the nanotubes. This result can be attributed to the formation of defects during the TCVD nanotubes synthesis process, as shown in Fig. S6 and Table S2.† TiO₂ ALD preferentially nucleate and grow at the defect sites on the CNT surface, resulting in a conformal coating and avoiding w-VA-CNTs pre-functionalization.

Along with deposition, the crystallinity of TiO₂ is highly modulated from amorphous to a crystalline phase with the variation of the deposition temperature. This behaviour was followed by GIXRD analysis, as shown in Fig. S7 and Table S3.† In Fig. S7a,† it is possible to observe the transition of amorphous to the crystalline structure, which is attained after the temperature increase from 100 °C to 200 °C. In the sample pattern obtained at 150 °C (Fig. 3a and b), a diffraction maximum starts appearing in the angular position (2θ) of 25.5°. This diffraction maximum can be indexed to the (101) plane of the tetragonal anatase phase structure, as can be corroborated by its similarity with the standard diffraction pattern of the anatase TiO₂ phase (JCPDS card 01-083-5914, see Fig. S7a†). Raman spectroscopy is also a powerful tool to accurately identify the distinct crystalline phases of materials, as well as their density of defects. Hence, the TiO₂ anatase and rutile phases can be identified by Raman spectroscopy²⁵ by inspecting their characteristic vibrational modes predicted according to the group theory. Anatase belongs to the spacial group D_{4h} (I_{41}/amd) and exhibits 6 modes that are active in Raman, $A_{1g} + 2B_{1g} + 3E_g$, which occur at about 143 cm⁻¹ (E_g), 198 cm⁻¹ (E_g), 395 cm⁻¹ (B_{2g}), 512 cm⁻¹ (A_{1g}), 518 cm⁻¹ (B_{1g}), 639 cm⁻¹ (E_g),²⁶ were indeed identified in the Raman spectra of the present samples. Fig. 3c and d depicts the Raman spectra showing well-resolved anatase vibrational modes for the samples with TiO₂ deposited at 150, 200 and 250 °C. The anatase TiO₂ crystalline phase shows a prominently intense, low-frequency mode at ~148 cm⁻¹ (Table S4†). Such high intensity of this low-frequency mode is not observed in the case of amorphous TiO₂. Neither rutile TiO₂ nor other phases were detected in the analysed samples. The bands at 1342 cm⁻¹ and 1580 cm⁻¹ are assigned to the D and G bands, respectively, of the w-VA-CNTs



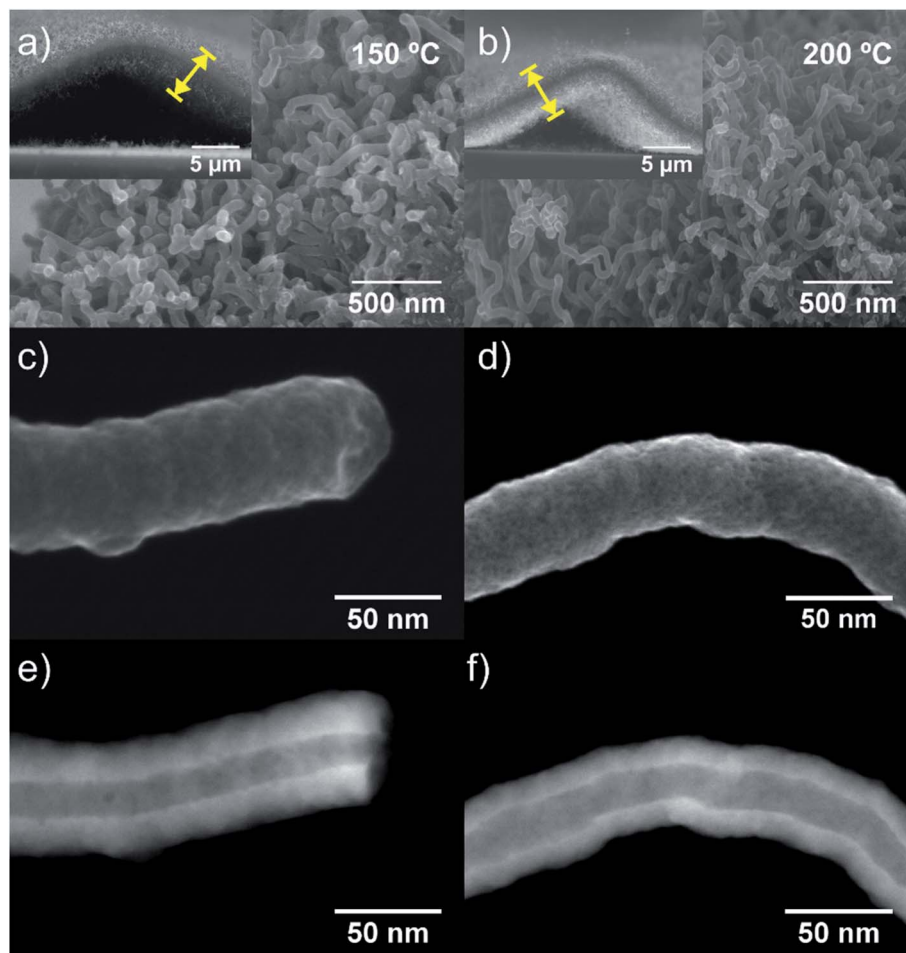


Fig. 2 Cross-sectional SEM images (a and b) of the $\text{TiO}_2/\text{w-VA-CNTs}$ nanocomposites after 200 ALD cycles at 150 °C and 200 °C, respectively. The insets are the low magnification cross-section SEM images of one individual wave-like pattern comprised of the VA-CNTs with an underneath hollow cavity. SE-STEM mode images (c and d) and corresponding ZC-STEM mode images (e and f) of an individual coated nanotube with TiO_2 after 200 ALD cycles. The nanotubes' array height is estimated to be $2.3 \pm 0.1 \mu\text{m}$.

array. Moreover, the observed D and G bands are a characteristic feature of the multiwalled carbon nanotubes. For comparison purposes, the Raman spectrum of an uncoated w-VA-CNTs array is depicted in Fig. S6.†

Independently of the film thickness, all the $\text{TiO}_2/\text{w-VA-CNTs}$ nanocomposites exhibit an intensity of the D band higher than the G, indicating the presence of disorder and/or defects in the CNTs. The TiO_2 film thickness was estimated to be 12.7 nm, 11.2 nm, and 11.1 nm for the deposition temperatures of 150 °C, 200 °C and 250 °C, respectively. These values were determined from the TE-STEM mode image depicted in Fig. S8.† On the other hand, the plot in Fig. S9† reveals the TiO_2 thickness evolution as a function of the deposition temperature, allowing the growth rate (*i.e.*, GPC) determination of the TiO_2 ALD process, as shown in Table S5.† The GPC remains constant in the 200–250 °C region, suggesting that the TTIP and H_2O precursors reacted at the surface of the nanotubes *via* a self-limiting reaction. For comparison purposes, the TiO_2 film thickness deposited at 200 °C on Si (100) was estimated to be 17.7 nm by the XRR technique (Fig. S10 and Table S5†), leading

to a slight increase in GPC on a flat substrate. Considering the high surface area of the non-functionalized w-VA-CNTs, the observed difference in the GPC values is not unusual since the ALD precursors need to infiltrate from the top to the bottom of the w-VA-CNTs array structure. The observed decline of GPC can be caused by the increasing desorption of –OH groups with higher temperatures at *ca.* 300 °C. To better understand this phenomenon, the number of ALD cycles was increased from 200 to 400 while maintaining the deposition temperature at 300 °C. In this case, the TiO_2 thickness was 4.6 nm, slightly lower than the estimated for the 200 ALD cycles, *i.e.*, 5.6 nm. The explanation for the decreasing trend is the reduction in the –OH group concentration of the TiO_2 surface. As expected, in the H_2O -based process, where –OH groups are the reactive sites, the growth rate decreases with increasing growth temperature from 100 to 200 °C. As reported in the literature, the growth rate using TTIP precursor with H_2O was found to be about 0.05–0.06 nm per cycle,¹⁵ which is indeed observed in the present work for the deposition of TiO_2 ALD with the used precursors' combination. In addition, the growth rates of TiO_2 films on



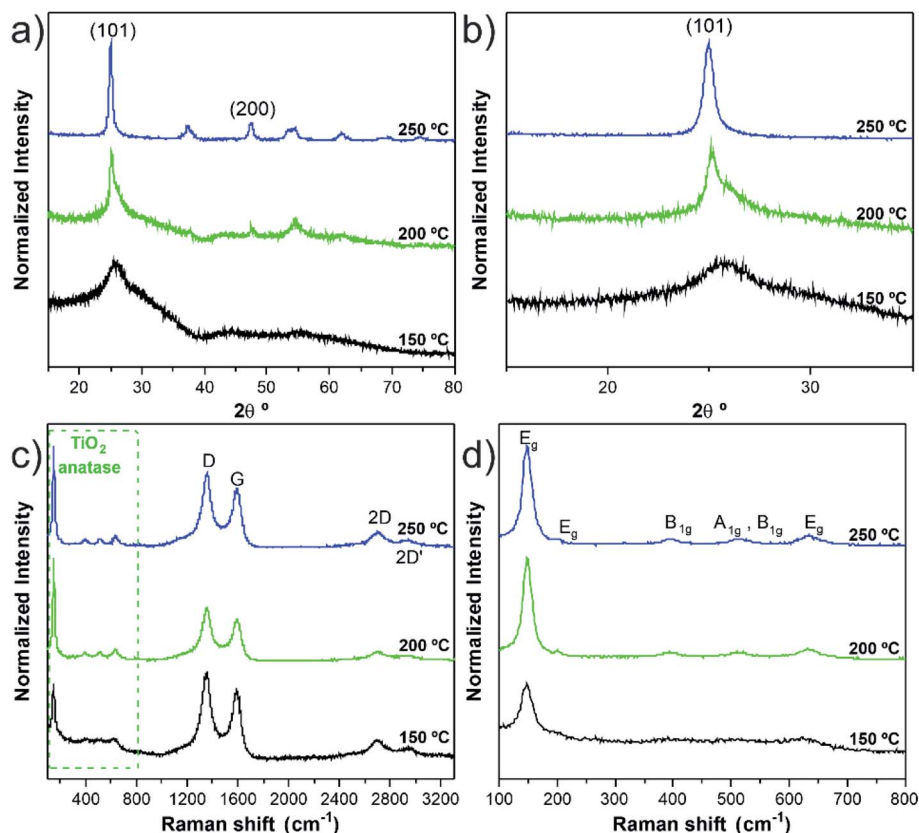


Fig. 3 Representative GIXRD diffraction patterns (a) and GIXRD diffraction pattern in the range of (2θ) 23–28°(b), Raman spectra (c) and (d) enlarged Raman spectra in the range of 100–800 cm^{-1} of $\text{TiO}_2/\text{w-VA-CNTs}$ nanocomposites after 200 ALD cycles at 150, 200 and 250 °C. For GIXRD, the JCPD-01-083-5914 data card was used as the reference. TiO_2 thickness range between 12.7 and 11.2 nm from lower to higher deposition temperatures.

nanotubes found in the literature are summarized in Table S6.† Therefore, it can be confirmed that the deposition temperature plays a more critical role in influencing the type of TiO_2 phase formation rather than the film's thickness.

The TiO_2 films were also analysed by optical absorption. Fig. 4 depicts the UV-Vis absorbance spectra for the 150 °C and 200 °C TiO_2 thin films. The most significant differences in the optical response of the samples reside mainly in their absorption spectra. It is worth mentioning that, as can be seen in Fig. S7,† the amorphous 100 °C TiO_2 film exhibits a similar absorption spectrum as the one presented for the 150 °C sample. Inspecting Fig. 4, while the 150 °C TiO_2 film display an onset absorption near 360 nm (~ 3.44 eV), the 200 °C crystalline sample starts to absorb light at wavelengths below ~ 380 nm (~ 3.26 eV). This value is in line with the expected value for the TiO_2 anatase bandgap energy at RT (~ 3.2 eV).²²

The PL spectroscopy has been applied to unravel the optically active centres and discriminate between processes sensitive to surface termination and bulk processes. The PL and PLE spectra were recorded at RT for the synthesized w-VA-CNTs after 200 ALD cycles at 150 °C and 200 °C, as shown in Fig. 4. With the above TiO_2 bandgap excitation, the PL spectra of the films on w-VA-CNTs exhibit a broad unstructured emission band centred in the orange spectral region at ~ 534 nm (2.32 eV), which is

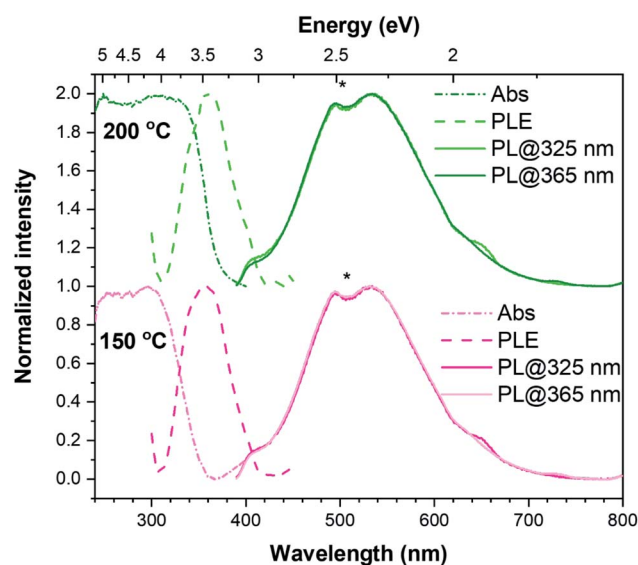


Fig. 4 UV-Vis absorbance (dash-dot line), PLE (dashed line) and RT PL (full line) spectra of $\text{TiO}_2/\text{w-VA-CNTs}$ nanocomposites after 200 ALD cycles at 150 °C (lower spectra) and 200 °C (upper spectra); the * denotes an artifact of the detection system. The PL spectra were acquired under two different excitation wavelengths, 325 nm and 365 nm (maximum of the PLE band).

likely to be due to an overlapping of emitting centres as reported in the literature.^{27,28} The spectral shape and peak position of the emission band was seen to be similar for all the analysed sample (including the one prepared at 100 °C), with only some differences in the overall intensity. As well, the spectral shape was kept when probed with different excitation energies, while the intensity was seen to slightly change with the excitation employed (the spectra in Fig. 4 are normalized to highlight the similarity in the PL spectral shape), being consistently higher when the 365 nm (~ 3.4 eV) was used, which corresponds to the maximum of the excitation band identified in the PLE assessment. When monitored at the band maximum, the PLE spectra of both samples reveal that the emission is preferentially excited for wavelengths shorter than 425 nm (~ 2.917 eV), with a maximum at 360 nm (~ 3.444 eV), rather than through the material's bandgap. This excitation band differs from what was observed in the absorbance spectra and is equal in both cases depicted in Fig. 4, indicating that this feature is independent of the structural properties of the samples and is likely related to a localized optical centre. Broad bands peaked in the yellow/orange spectral region and with similar spectral shapes to those observed here have been previously reported in the literature for TiO₂ anatase.^{28–32}

The emission is frequently attributed to an overlap of emitting centres, including the recombination of self-trapped excitons (STE), either involving free electrons or electrons trapped in oxygen vacancies (V_O).^{27,33} The STEs are formed when electrons are excited to the conduction band by photons with energies higher than the bandgap and then relax to the bottom of the conduction band, forming polarons that are highly localized by strong interaction with holes.³² STEs can occur in polar semiconductors with electron–phonon strong coupling.²⁹ On the other hand, according to Pallotti *et al.*,²⁹ the origin of such a yellow PL band does not involve STEs or donor–acceptor pair recombination. Instead, it is associated with recombining the conduction band electrons with trapped holes localized at V_O sites (F-centres) or Ti sites adjacent to V_O. Radiative recombination between trapped electrons and valence band holes may also contribute to this broad emission, however being more

frequently associated with transitions in the orange/red spectral region and when below-bandgap excitation is employed, with which excitons cannot be formed.²⁹

Moreover, in nanocrystals, like the ones analysed here, some studies suggest that radiative recombination can be mediated by surface states.³⁰ Indeed, recombination processes involving surface and trap states are pointed out as possible contributions to anatase PL spectra, particularly in the case of samples with large specific surface areas.²⁹ Nevertheless, it is important to bear in mind that more than one of these (and other) contributions may play a role in the observed broad PL band. For instance, electronic surface states related to the adsorbed species on the surface of TiO₂ may also participate in radiative recombination in this spectral region. An example is the presence of the surface –OH groups related to Ti–OH, as attested by the XPS data (see Fig. 5b). Such defects can create surface traps either for electrons or holes, which have also been associated with the PL broad emissions.^{34,35}

The information regarding the chemical and bonding environment of TiO₂/w-VA-CNTs after 200 ALD cycles at 200 °C was ascertained using XPS (Fig. 5). This nanocomposite presents the highest photocatalytic activity, described in detail in the next section. The XPS survey spectra are shown in Fig. S11† exhibit three main peaks attributed to Ti, O, and C elements present in the nanocomposite. The high intensity of the Ti 2p peak compared to that of the C 1s peak can be assigned to the TiO₂ film on the nanotubes' surface. There is no evidence of chemical contamination with other elements. The core-level spectrum of Ti 2p was investigated to unveil the oxidation state of the Ti element. After deconvolution, the measured energies for Ti⁴⁺ bonding were 458.2 eV for Ti 2p_{3/2} and 463.9 eV for Ti 2p_{1/2} (Table S7†). The difference of 5.7 eV between Ti 2p_{3/2} and Ti 2p_{1/2} peaks indicates that Ti is present mostly as Ti⁴⁺, corresponding to TiO₂, where Ti 2p_{1/2} is broader than the Ti 2p_{3/2} (ref. 36) with Ti/O atomic ratio of 0.51 (Table S8†). The O 1s spectrum shows two peaks, among which the lower binding energy peak located at 529.8 eV is attributed to oxygen bound (O–Ti) in TiO₂ and the peak at higher binding energy at 532.5 eV to surface –OH groups (Ti–OH).³⁶

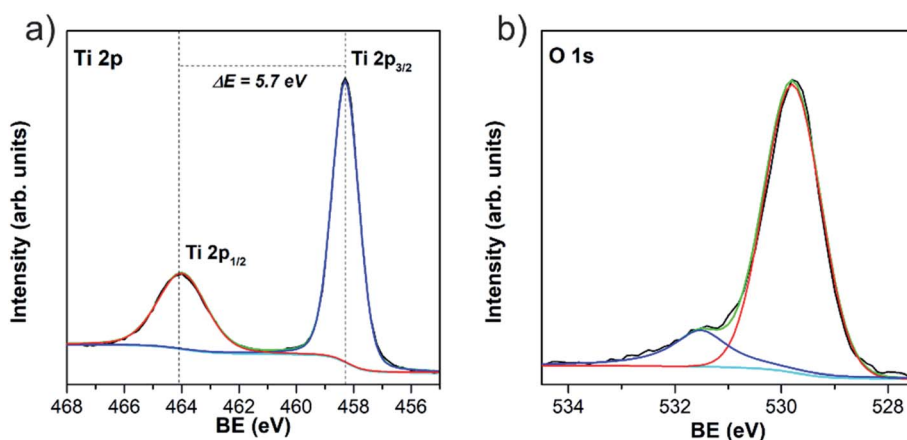


Fig. 5 XPS core-level spectra of Ti 2p (a) and O 1s (b) (BE stands for binding energy).

The presence of $-OH$ groups on the TiO_2 surface was also emphasized by measuring the water contact angle (θ_c). A θ_c value of 0° was observed where a thin water-film is formed, which directly impacted better wettability compared to the uncoated w-VA-CNTs (Fig. S12[†]). Such contact angle value corroborates the analysis O 1s core-level spectrum performed with the XPS studies. According to these results, the obtained coatings are much likely composed of pure TiO_2 films and the existence of $-OH$ groups on the TiO_2 surface cannot only enhance the water dispersibility but also promote RhB molecule dye sensitization.

Photocatalytic activity of TiO_2 /VA-CNTs and TiO_2 /w-VA-CNTs structures

The photocatalytic response arising from the as-prepared nanocomposites was evaluated by degrading RhB under UV light excitation. First, the variation of the ALD number of cycles (*i.e.*, 50, 100, 200 and 400 cycles at $200^\circ C$) is used to clearly show the effects of the TiO_2 loading onto w-VA-CNTs on the photodegradation activity. As shown in Fig. 6a, the increase in TiO_2 load shows a positive influence on the photodegradation efficiency supported by the decrease of the characteristic RhB absorption band intensity. Hence, the further addition of TiO_2 does not lead to the enhancement of degradation efficiency. To further understand the contribution of each component to the photocatalytic performance, the bare Si/SiO₂ substrate and TiO_2 thin film deposited on Si/SiO₂ substrate were also tested in photodegradation studies, as shown in Fig. 6b.

The wave-like feature of the w-VA-CNTs array was revealed to be the most favourable for enhancing the TiO_2 photocatalytic activity. Nevertheless, both types of VA-CNTs arrays are suitable for improving the TiO_2 photocatalytic activity due to the formation of the nanocomposite that presents attractive properties like high surface area and highly ordered geometry. From the EDS elemental maps, it is possible to observe that the Ti is uniformly distributed on the surface of the nanotubes of both VA-CNTs arrays, as shown in Fig. S13.[†] In this context, a negligible activity of the bare Si/SiO₂ substrate is observed in contrast to the TiO_2 thin film

(17.7 nm thickness) deposited directly on Si/SiO₂ substrate, which achieves a slightly higher activity ($\approx 10\%$ and $\approx 25\%$, respectively). As expected, in the absence of a TiO_2 photocatalyst, no degradation of RhB was observed. It is also clear that the VA-CNTs array surface area is much larger than the planar Si/SiO₂ substrate, emphasizing the role of the photocatalyst support geometry. To summarize, in the experiments conducted under UV irradiation, it was found that the photocatalytic efficiency of TiO_2 ALD films on VA-CNTs improves with film thickness until reaching saturation at about 11.2 nm (*i.e.*, 200 ALD cycles).

The w-VA-CNTs coated with 200 TiO_2 ALD cycles were chosen for further studies because it exhibits the highest photodegradation efficiency (55% of RhB degradation). Interestingly, in previous work by our group,²⁰ we were able to prepare ZnO/VA-CNTs nanocomposites for the photodegradation of RhB aqueous solution, where 58% of RhB degradation was reached after 240 min UV illumination with the material obtained from 100 ALD cycles of ZnO at $200^\circ C$, which corresponds to a ZnO thickness of 13.0 nm. We clearly notice of approximately the same thickness, both oxides present similar photocatalytic activity. The difference in the thickness values (*i.e.*, number of ALD cycles) is explained by the growth mechanism and precursors used to obtain TiO_2 (TTIP/ H_2O) and ZnO (DEZ/ H_2O). Additionally, these findings can be understood considering that the photocatalytic process is a photon assisted chemical reaction taking place at the material's surface, making it strongly affected by the exposed surface area, and the improved photocatalytic efficiency can be attributed to the synergistic effect between the metal oxides and carbon nanotubes, rather than its individual components.²⁰ In this context, the 200 ALD cycles were kept fixed while the deposition temperature was varied from $100^\circ C$ to $300^\circ C$ to evaluate the impact of the amorphous and crystalline nature of the TiO_2 films on the photocatalytic activity towards RhB degradation. Fig. 7a shows a comparison of the photodegradation performance of various nanocomposite samples at various deposition temperatures. In order to compare the efficiencies, the stability of the RhB dye solution

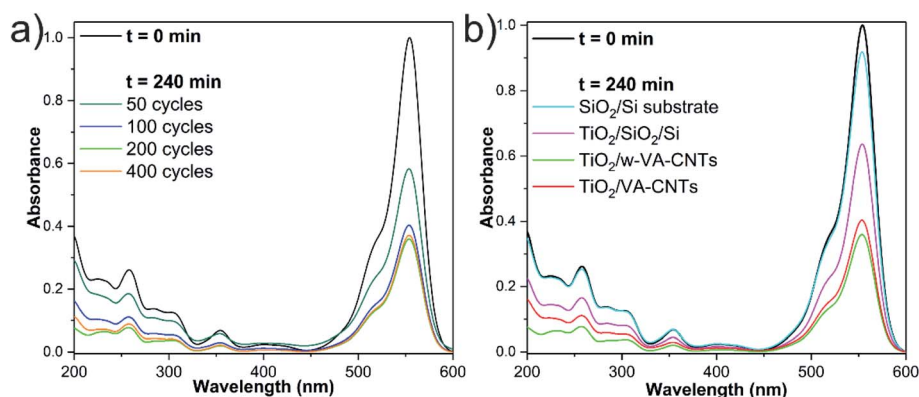


Fig. 6 UV-Vis absorbance spectra showing the variation of the RhB absorption intensity with the ALD number of cycles at $200^\circ C$ (a) and type of substrates (b) after 240 min of irradiation time.



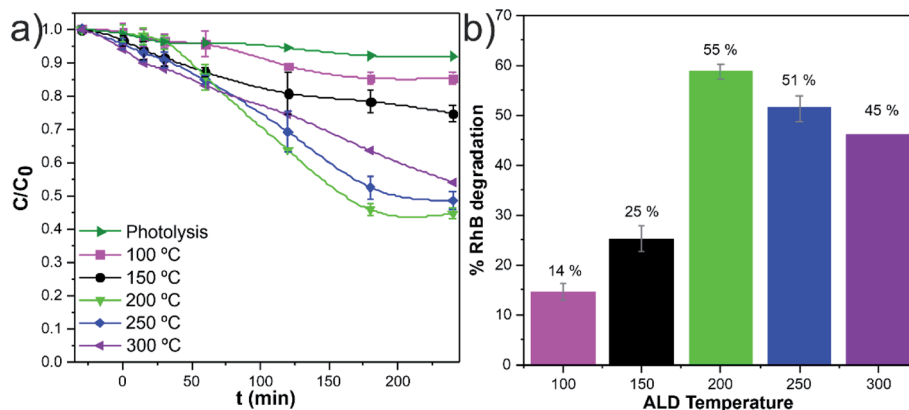


Fig. 7 Evolution of the normalized concentration of RhB (C/C_0) vs. time of UV illumination of the samples obtained at various deposition temperatures (a) and corresponding photocatalytic degradation percentages of RhB at the end of 240 min of irradiation (b).

was also examined under identical conditions, so-called photolysis, around 8% after 240 min of irradiation time. It is clear that the anatase TiO_2 at 200 °C nanocomposites exhibited a higher photocatalytic activity than the other nanocomposites, in particular for the nanocomposites with amorphous TiO_2 . This finding is further emphasized in Fig. 7b, where the percentages of RhB degradation are depicted.

A pseudo-first-order rate law usually describes the photo-degradation of most organic compounds following the Langmuir–Hinshelwood model.³⁷ The slope of $-\ln(C_0/C)$ plotted versus irradiation time (min) corresponds to the pseudo-first-order apparent rate constant (k_{app} , Fig. 8a). The k_{app} values (Fig. 8b) suggest that the RhB degradation was mainly carried out by photocatalysis rather than photolysis. The increase of the k_{app} values represents an enhancement in the degradation rate of the RhB dye molecule. Among these photocatalytic active nanocomposites, the anatase $\text{TiO}_2/\text{w-VA-CNTs}$ obtained at 250 °C showed the highest reaction rate, after 60 min, thus exhibiting the highest percentage of degradation of RhB as compared to the other nanocomposites (more details in Fig. S14†).

Recyclability tests

The remarkable photocatalytic efficiency of the nanocomposites was demonstrated by the degradation of RhB in an aqueous solution under UV light irradiation. The reusability is an essential factor to assess the stability and for the photocatalyst practical application. The photocatalytic tests did not significantly modify the anatase crystalline TiO_2 structure of the nanocomposite (*i.e.*, phase stability), supported by the comparison of the GIXRD patterns and Raman spectra before and after photocatalysis, as given in Fig. 9a and b. In addition, the nanocomposite remained mechanically attached to the support, as shown in Fig. S15.† However, photocatalytic degradation percentage gradually decreased after several RhB discoloration runs (Fig. 9c and d). A possible explanation for this phenomenon could be the poisoning effect caused by the adsorption of the degraded products that can block part of the catalytic reaction sites.³⁸ The loss of catalyst during the recyclability tests is another hypothesis for the decrease of the degradation percentage. In our case, this is an unlikely hypothesis since the estimated Ti/C ratio (at%) values from the SEM/EDS analysis (Table S9†) showed similar values.

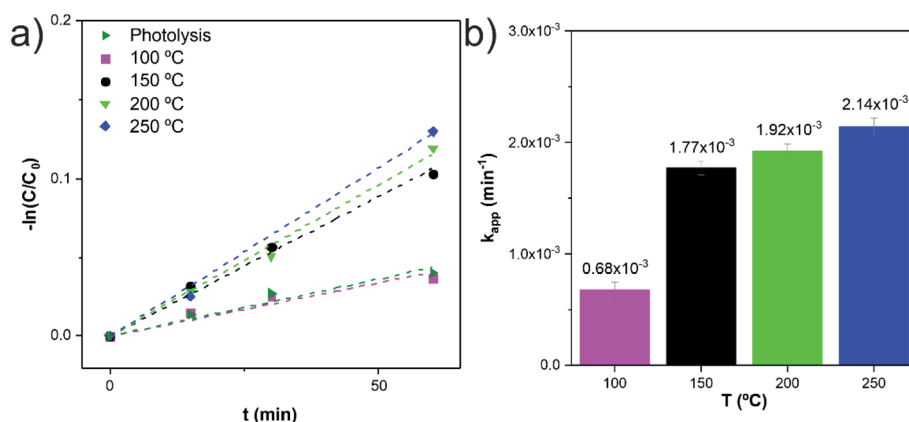


Fig. 8 Reaction kinetics (linear transform, $-\ln C/C_0$ vs. t) (a) and corresponding reaction rate constants (k_{app}) (b).

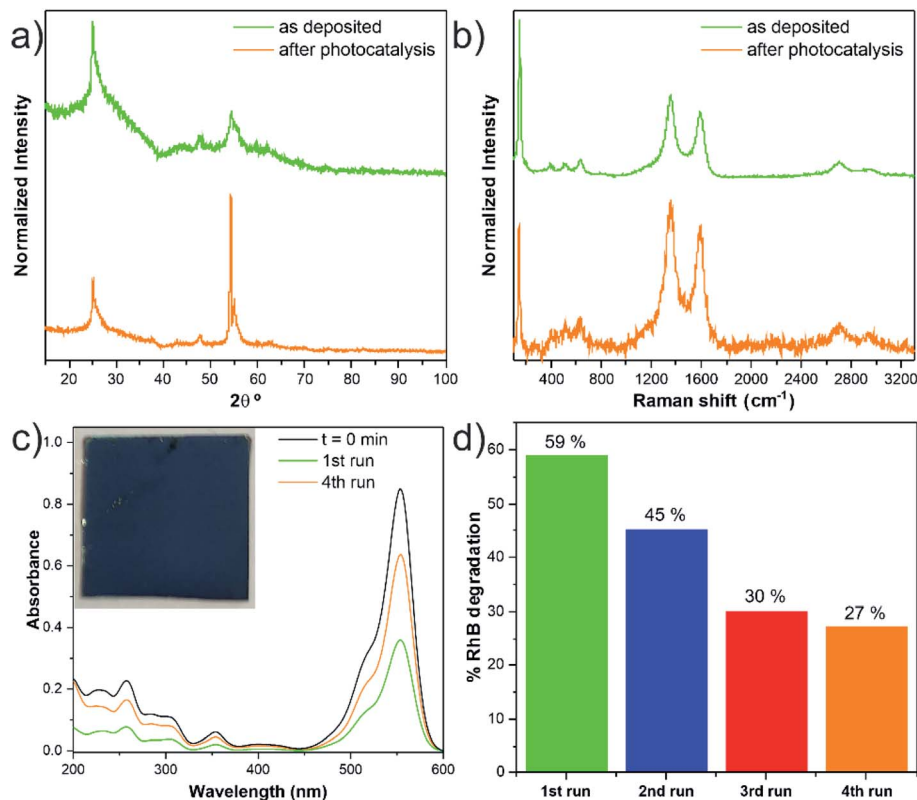


Fig. 9 GIXRD pattern (a) and Raman spectra (b) before and after photodegradation tests. UV-vis absorbance spectra of the RhB (c) and photocatalytic degradation percentage of w-VA-CNTs (d). The inset in (c) shows a digital photograph of the nanocomposite where the measurements were acquired.

Conclusions

The $\text{TiO}_2/\text{w-VA-CNTs}$ nanocomposites present a core-shell and hierarchically structural design, which rationally combines the advantages of structural manipulation and multi-material composition engineering. The results demonstrate that the deposition temperature can effectively control the TiO_2 phase composition.

The TiO_2 films presented different photocatalytic yields, suggesting a minimum and a maximum limiting thickness (*i.e.*, number of ALD cycles) for maximizing the photocatalytic activity.

The $\text{TiO}_2/\text{w-VA-CNTs}$ nanocomposite after 200 ALD cycles at 200 °C was revealed as a stable photocatalyst as no considerable change occurred in its morphology and chemical structure after four cyclic usages.

The removal process of dyes and other organic pollutants is controlled by the value of bandgap energy and the surface area, and the density of adsorption active sites (surface hydroxyl groups) of anatase TiO_2 film. The immobilization of the TiO_2 photocatalyst on the w-VA-CNTs substrates is a practical advantage, while the suspended photocatalyst needs to be separated after the purification, which can be considered a limitation. So, it could be concluded that the structural properties of TiO_2 had some impact on their photocatalytic activity. Many applications can benefit from TiO_2

materials with fine-tuned structural and surface characteristics and the synergy between the components in the nanocomposite.

Finally, the efficient photodegradation of organic pollutants remains challenging and strongly depends on the surface morphological properties of the photocatalyst.

Author contributions

Inês E. Oliveira: conceptualization, methodology, investigation, validation, formal analysis, writing – original draft, and writing – review and editing; Ricardo M. Silva: methodology, formal analysis, writing – review and editing; Joana Rodrigues: formal analysis, writing – review and editing; Maria R. Correia: formal analysis, writing – review and editing; Teresa Monteiro: formal analysis, writing – review and editing; Joaquim L. Faria: conceptualization, funding acquisition, writing – review and editing; Rui F. Silva: conceptualization, methodology, validation, supervision, resources, funding acquisition, writing – review and editing; Cláudia G. Silva: conceptualization, methodology, validation, supervision, resources, funding acquisition, writing – review and editing.

Conflicts of interest

There are no conflicts to declare.



Acknowledgements

This work was developed within the scope of the project CICECO-Aveiro Institute of Materials, UIDB/50011/2020 & UIDP/50011/2020, financed by national funds through the FCT/MEC. This work was financially supported by LA/P/0045/2020 (ALiCE), UIDB/50020/2020 and UIDP/50020/2020 (LSRE-LCM), funded by national funds through FCT/MCTES (PIDDAC). I. E. O. acknowledges FCT for the research grant 2020.06213.BD. We are indebted to Marta C. Ferro for technical assistance and advice with scanning transmission electron microscopy studies. J. Rodrigues, M. R. Correia, and T. Monteiro also acknowledge the project i3N, UIDB/50025/2020 & UIDP/50025/2020.

Notes and references

- 1 B. J. O'Neill, D. H. K. Jackson, J. Lee, C. Canlas, P. C. Stair, C. L. Marshall, *et al.* Catalyst Design with Atomic Layer Deposition, *ACS Catal.*, 2015, **5**(3), 1804–1825.
- 2 N. K. R. Eswar, S. A. Singh and J. Heo, Atomic layer deposited photocatalysts: comprehensive review on viable fabrication routes and reactor design approaches for photo-mediated redox reactions, *J. Mater. Chem. A*, 2019, **7**(30), 17703–17734.
- 3 Z. Xing, J. Zhang, J. Cui, J. Yin, T. Zhao, J. Kuang, *et al.* Recent advances in floating TiO₂-based photocatalysts for environmental application, *Appl. Catal., B*, 2018, **225**, 452–467.
- 4 A. Ajmal, I. Majeed, R. N. Malik, H. Idriss and M. A. Nadeem, Principles and mechanisms of photocatalytic dye degradation on TiO₂ based photocatalysts: a comparative overview, *RSC Adv.*, 2014, **4**(70), 37003–37026.
- 5 K. R. Reddy, M. S. Jyothi, A. V. Raghu, V. Sadhu, S. Naveen and T. M. Aminabhavi, Chapter 6 Nanocarbons-Supported and Polymers-Supported Titanium Dioxide Nanostructures as Efficient Photocatalysts for Remediation of Contaminated Wastewater and Hydrogen Production, in *Nanophotocatalysis and Environmental Applications*, 30, ed. A. A. M. Inamuddin and E. Lichtfouse, 1st edn, Switzerland, Cham, Springer, 2020, pp. 139–69.
- 6 K. R. Reddy, K. V. Karthik, S. B. B. Prasad, S. K. Soni, H. M. Jeong and A. V. Raghu, Enhanced photocatalytic activity of nanostructured titanium dioxide/polyaniline hybrid photocatalysts, *Polyhedron*, 2016, **120**, 169–174.
- 7 C. Guerra-Núñez, Y. C. Zhang, M. Li, V. Chawla, R. Erni, J. Michler, *et al.* Morphology and crystallinity control of ultrathin TiO₂ layers deposited on carbon nanotubes by temperature-step atomic layer deposition, *Nanoscale*, 2015, **7**(24), 10622–10633.
- 8 M. J. Sampaio, R. R. N. Marques, P. B. Tavares, J. L. Faria, A. M. T. Silva and C. G. Silva, Tailoring the properties of immobilized titanium dioxide/carbon nanotube composites for photocatalytic water treatment, *J. Environ. Chem. Eng.*, 2013, **1**(4), 945–953.
- 9 R. R. N. Marques, M. J. Sampaio, P. M. Carrapiço, C. G. Silva, S. Morales-Torres, G. Dražić, *et al.* Photocatalytic degradation of caffeine: Developing solutions for emerging pollutants, *Catal. Today*, 2013, **209**, 108–115.
- 10 T. S. Natarajan, J. Y. Lee, H. C. Bajaj, W.-K. Jo and R. J. Tayade, Synthesis of multiwall carbon nanotubes/TiO₂ nanotube composites with enhanced photocatalytic decomposition efficiency, *Catal. Today*, 2017, **282**, 13–23.
- 11 Y. Chen, J. Qian, N. Wang, J. Xing and L. Liu, *In situ* synthesis of CNT/TiO₂ heterojunction nanocomposite and its efficient photocatalytic degradation of Rhodamine B dye, *Inorg. Chem. Commun.*, 2020, **119**, 108071.
- 12 J. Zhang, P. Zhou, J. Liu and J. Yu, New understanding of the difference of photocatalytic activity among anatase, rutile and brookite TiO₂, *Phys. Chem. Chem. Phys.*, 2014, **16**, 20382–20386.
- 13 M. Ritala, M. Leskelä, L. Niinistö and P. Haussalo, Titanium Isopropoxide as a Precursor in Atomic Layer Epitaxy of Titanium Dioxide Thin Films, *Chem. Mater.*, 1993, **5**, 1174–1181.
- 14 M. Ritala, M. Leskelä and E. Rauhala, Atomic Layer Epitaxy Growth of Titanium Dioxide Thin Films from Titanium Ethoxide, *Chem. Mater.*, 1994, **6**(4), 556–561.
- 15 J. Aarik, A. Aidla, T. Uustare, M. Ritala and M. Leskelä, Titanium isopropoxide as a precursor for atomic layer deposition: characterization of titanium dioxide growth process, *Appl. Surf. Sci.*, 2000, **161**(3), 385–395.
- 16 Y. C. Zhang, C. Guerra-Núñez, I. Utke, J. Michler, M. D. Rossell and R. Erni, Understanding and Controlling Nucleation and Growth of TiO₂ Deposited on Multiwalled Carbon Nanotubes by Atomic Layer Deposition, *J. Phys. Chem. C*, 2015, **119**(6), 3379–3387.
- 17 J. H. Feng, S. Xiong, Z. G. Wang, Z. L. Cui, S. P. Sun and Y. Wang, Atomic layer deposition of metal oxides on carbon nanotube fabrics for robust, hydrophilic ultrafiltration membranes, *J. Membr. Sci.*, 2018, **550**, 246–253.
- 18 X. B. Meng, M. N. Banis, D. S. Geng, X. F. Li, Y. Zhang, R. Y. Li, *et al.* Controllable atomic layer deposition of one-dimensional nanotubular TiO₂, *Appl. Surf. Sci.*, 2013, **266**, 132–140.
- 19 B. Q. Wang, J. Liu, Q. Sun, B. W. Xiao, R. Y. Li, T. K. Sham, *et al.* Titanium Dioxide/Lithium Phosphate Nanocomposite Derived from Atomic Layer Deposition as a High-Performance Anode for Lithium Ion Batteries, *Adv. Mater. Interfaces*, 2016, **3**(21), 1600369.
- 20 I. E. Oliveira, R. M. Silva, A. V. Girão, J. L. Faria, C. G. Silva and R. F. Silva, Facile Preparation of ZnO/CNTs Nanocomposites via ALD for Photocatalysis Applications, *Eur. J. Inorg. Chem.*, 2020, 1743–1750.
- 21 C. F. Holder and R. E. Schaak, Tutorial on Powder X-ray Diffraction for Characterizing Nanoscale Materials, *ACS Nano*, 2019, **13**(7), 7359–7365.
- 22 Z. Guo, F. Ambrosio and A. Pasquarello, Hole diffusion across leaky amorphous TiO₂ coating layers for catalytic water splitting at photoanodes, *J. Mater. Chem. A*, 2018, **6**(25), 11804–11810.
- 23 M. Stobiecka and M. Hepel, Multimodal coupling of optical transitions and plasmonic oscillations in rhodamine B modified gold nanoparticles, *Phys. Chem. Chem. Phys.*, 2011, **13**(3), 1131–1139.



- 24 S. H. Huang, S. Y. Liao, C. C. Wang, C. C. Kei, J. Y. Gan and T. P. Perng, Direct formation of anatase TiO₂ nanoparticles on carbon nanotubes by atomic layer deposition and their photocatalytic properties, *Nanotechnology*, 2016, **27**(40), 405702.
- 25 W. Ma, Z. Lu and M. Zhang, Investigation of structural transformations in nanophase titanium dioxide by Raman spectroscopy, *Appl. Phys. A*, 1998, **66**(6), 621–627.
- 26 S. P. S. Porto, P. A. Fleury and T. C. Damen, Raman Spectra of TiO₂, MgF₂, ZnF₂, FeF₂, and MnF₂, *Phys. Rev.*, 1967, **154**(2), 522–526.
- 27 K. Iijima, M. Goto, S. Enomoto, H. Kunugita, K. Ema, M. Tsukamoto, *et al.* Influence of oxygen vacancies on optical properties of anatase TiO₂ thin films, *J. Lumin.*, 2008, **128**(5–6), 911–913.
- 28 M. P. Graca, C. Nico, M. Peres, M. A. Valente and T. Monteiro, Study of the optical and dielectric properties of TiO₂ nanocrystals prepared by the Pechini method, *J. Nanosci. Nanotechnol.*, 2012, **12**(11), 8600–8606.
- 29 D. K. Pallotti, L. Passoni, P. Maddalena, F. Di Fonzo and S. Lettieri, Photoluminescence Mechanisms in Anatase and Rutile TiO₂, *J. Phys. Chem. C*, 2017, **121**(16), 9011–9021.
- 30 W. F. Zhang, M. S. Zhang, Z. Yin and Q. Chen, Photoluminescence in anatase titanium dioxide nanocrystals, *Appl. Phys. B: Lasers Opt.*, 2000, **70**(2), 261–265.
- 31 A. Suisalu, J. Aarik, H. Mändar and I. Sildos, Spectroscopic study of nanocrystalline TiO₂ thin films grown by atomic layer deposition, *Thin Solid Films*, 1998, **336**(1–2), 295–298.
- 32 H. Yoo, M. Kim, C. Bae, S. Lee, H. Kim, T. K. Ahn, *et al.* Understanding Photoluminescence of Monodispersed Crystalline Anatase TiO₂ Nanotube Arrays, *J. Phys. Chem. C*, 2014, **118**(18), 9726–9732.
- 33 I. Sildos, A. Suisalu, J. Aarik, T. Sekiya and S. Kurita, Self-trapped exciton emission in crystalline anatase, *J. Lumin.*, 2000, **87–89**, 290–292.
- 34 E. Konstantinova, J. Weidmann and T. Dittrich, Influence of Adsorbed Water and Oxygen on the Photoluminescence and EPR of Por-TiO₂ (Anatase), *J. Porous Mater.*, 2000, **7**, 389–392.
- 35 C. Di Valentin and A. Selloni, Bulk and Surface Polarons in Photoexcited Anatase TiO₂, *J. Phys. Chem. Lett.*, 2011, **2**(17), 2223–2228.
- 36 V. V. Atuchin, V. G. Kesler, N. V. Pervukhina and Z. Zhang, Ti 2p and O 1s core levels and chemical bonding in titanium-bearing oxides, *J. Electron Spectrosc. Relat. Phenom.*, 2006, **152**(1–2), 18–24.
- 37 Y. Lin, C. Ferronato, N. Deng, F. Wu and J.-M. Chovelon, Photocatalytic degradation of methylparaben by TiO₂: Multivariable experimental design and mechanism, *Appl. Catal., B*, 2009, **88**(1–2), 32–41.
- 38 M. Argyle and C. Bartholomew, Heterogeneous Catalyst Deactivation and Regeneration: A Review, *Catalysts*, 2015, **5**(1), 145–269.

